Simulating Correlations of Structured Spontaneously Down-Converted Photon Pairs

Sivan Trajtenberg-Mills, Aviv Karnieli, Noa Voloch-Bloch, Eli Megidish, Hagai S. Eisenberg, and Ady Arie*

Introducing structure into photon pair generation via spontaneous parametric down-conversion (SPDC) is shown to be useful for controlling the output state and exploiting new degrees of freedom for quantum technologies. This paper presents a new method for simulating first- and second-order correlations of the down-converted photons in the presence of structured pump beams and shaped nonlinear photonic crystals. This method is nonperturbative, and thus accounts for high-order effects, and can be made very efficient using parallel computing. Experimental results of photodetection and coincidence rates in complex spatial configurations are recovered quantitatively by this method. These include SPDC in 2D nonlinear photonic crystals, as well as with structured light beams such as Laguerre Gaussian and Hermite Gaussian beams. This simulation method reveals conservation rules for the down-converted signal and idler beams that depend on the nonlinear crystal modulation pattern and the pump shape. This scheme can facilitate the design of nonlinear crystals and pumping conditions for generating non-classical light with pre-defined properties.

1. Introduction

The generation of non-classical states of light is ubiquitous in applications of quantum information, such as quantum cryptography,[1] quantum communication,[2] and quantum computation.[3] One of the leading methods for generating non-classical light is spontaneous parametric down conversion (SPDC),[4] a second-order nonlinear optical process in which one pump photon from a laser source spontaneously converts into two sub-harmonic photons (also called bi-photons) with lower energy. The generated photons can be naturally entangled in many degrees of freedom, making SPDC useful as a bright source of entangled photons. The process is attractive because it is well understood, easy to implement, and efficiently creates bi-photons in well-defined spatiotemporal modes.

The introduction of structure into SPDC was upgraded by the progress in quasi phase-matching (QPM), based mainly on electric field poling technology of ferroelectric crystals,[5,6] and by the wide availability of spatial light modulators (SLMs) for beam shaping. New and sophisticated crystal configurations enabled delicate control of the spatial properties of the spontaneously generated beams[7] Torres et al.[8] showed how modulated crystals can shape the generated photons by using a QPM process in crystals with defects and a curved modulation. Engineered nonlinear crystals were also studied for on-chip steering of entangled photons,[9] and periodic 2D crystals were used to create beam-like path entangled and polarization-entangled photons.[10–13]

SPDC is not limited to plane-wave-like beams only and was widely studied with structured pump beams,[14] such as diverging pump beams,[15–18] Laguerre Gaussian beams[19–21] and Hermite Gaussian beams.[22,23] Using structured light in SPDC also enables the creation of higher dimensional entanglement, for instance by employing the orbital angular momentum (OAM) as an additional degree of freedom for the photons.[24–28] The twin photons created in the process have been shown to inherit the spatial properties of the pump,[15] a property useful for quantum imaging.[29] This trait was also exploited for optimizing the coupling of the output photons to optical fibers.[30–32] Structuring both the pump light field and the nonlinear crystal further increases the possibilities for entanglement, and in this context, crystals with a fork-shaped modulation, pumped by vortex beams, were studied[33,34] as sources for entangled photons carrying OAM.[27]

The spatial distribution of the down-converted photons is often approximately predicted by wave vector diagram calculations. Unfortunately, these calculations do not give any information on the transverse width of the distribution or on higher-order

S. Trajtenberg-Mills, A. Karnieli
Sackler School of Physics
Faculty of Exact Sciences
Tel Aviv University
Tel Aviv 69978, Israel
E-mail: sivantra@mail.tau.ac.il

Dr. N. Voloch-Bloch, Dr. E. Megidish, Prof. H. S. Eisenberg
Racah Institute of Physics
Hebrew University of Jerusalem
Jerusalem 91904, Israel

Prof. A. Arie
School of Electrical Engineering
Fleischman Faculty of Engineering
Tel Aviv University
Tel Aviv 69978, Israel

The ORCID identification number(s) for the author(s) of this article can be found under https://doi.org/10.1002/lpor.201900321

DOI: 10.1002/lpor.201900321

effects. Also, they are unsuitable for complex crystals, with spatially varying nonlinearity, or for predicting the effect of simultaneous coupling between different modes. Similarly, the employment of the analytical solution for structured pump beams is most suitable for modal solutions of the wave equation (such as Hermite–Gauss[35] or Laguerre–Gauss[36]), but less so for general wavefronts.[37,38] Numerical solutions of SPDC are very rare, and were employed so far only for birefringent phase-matching in homogenous bulk crystals[39,40] and rarely for periodically poled crystals,[41] but never involving complex crystal structures.

In this paper we present a new simulation method, enabling to calculate the first-order and second-order correlation functions for the down-converted signal and idler photons. In Section 2, we show that the first-order correlation function can be numerically calculated by solving four coupled wave equations, using multiple random samples of classical input noise that simulates the quantum vacuum. We test this formulation by calculating the first-order correlation function of an SPDC process in a 2D nonlinear photonic crystal. Second-order correlations are derived in Section 3, and are then tested in a simple case of degenerate SPDC in a 1D periodically poled crystal. In Section 4, we study first- and second-order correlations for more advanced cases of structured light—decomposed into either the Hermite–Gauss or the Laguerre–Gauss basis, as well as for structured, fork-shaped nonlinear crystals. The results are summarized in Section 5.

2. Spatial Distribution of SPDC: First-Order Correlations

Correlations between photons in quantum optics is an important measure for establishing their quantum behavior, and enables to distinguish between different states of light, such as coherent states or number states (bunched or anti-bunched).[42] In the slowly varying envelope approximation (SVEA), and under the paraxial approximation, considering correlation at equal times ($t = t'$) and at the same detection plane ($z = z'$), the first-order correlation function of a wavefunction $|\psi\rangle$ can be written as

$$G^{(1)}_{i,j}\left(\mathbf{r}_T, \mathbf{r}'_T\right) = \left\langle \psi | \phi^{\dagger}_i(\mathbf{r}_T)\phi_j\left(\mathbf{r}'_T\right)|\psi\right\rangle \tag{1}$$

where $\phi_i(\mathbf{r}) = \sum_{\mathbf{q}} \frac{e^{i\mathbf{q}\cdot\mathbf{r}}}{\sqrt{V}} a_{\mathbf{k}_i+\mathbf{q}}$ is the paraxial envelope operator[42] around a carrier with a wavevector $\mathbf{k}_i$ (the index i denotes the carrier frequency ω_i and in general also the polarization state), $a_{\mathbf{k}_i+\mathbf{q}}$ is the annihilation operator, annihilating a photon in mode $\mathbf{k}_i + \mathbf{q}$ with $\mathbf{q}$ being the paraxial wave vectors satisfying $|\mathbf{q}| \ll |\mathbf{k}_i|$. This operator annihilates a photon at position $\mathbf{r}$, and is the Fourier transform of the annihilation operator. The first-order correlation measures the field autocorrelation among different frequencies (ω_i, ω_j) and transverse positions $(\mathbf{r}_T, \mathbf{r}'_T)$. Its diagonal elements (i.e., $i = j$ and $\mathbf{r}_T = \mathbf{r}'_T$) denote the probability of finding one photon at frequency ω_i and in position $\mathbf{r}_T$, and is the expectation value of the number density operator.

In the case of SPDC, the initial state is vacuum $|\psi\rangle = |0\rangle$; hence, the operators can only couple the vacuum state to any single-photon state in mode $\mathbf{k}$, $|1_{\mathbf{k}}\rangle$, so now we write the first-order correlation function as

$$G^{(1)}_{i,j}(\mathbf{r}_T, \mathbf{r}'_T) = \sum_{\mathbf{k}} \left\langle 0|\phi^{\dagger}_i(\mathbf{r}_T)|1_{\mathbf{k}}\right\rangle \left\langle 1_{\mathbf{k}}|\phi_j(\mathbf{r}'_T)|0\right\rangle \tag{2}$$

This implies that in order to compute it, one must trace over all possible single photon modes $\mathbf{k}$, something that can be numerically tedious. Instead, it is possible to approximate this sum by tracing over a large number N of independent "white noise" modes $|\mathbf{k}^{(n)}_{\text{rand}}\rangle$ $(n = 1 \ldots N)$, defined as

$$|\mathbf{k}^{(n)}_{\text{rand}}\rangle = \sum_{\mathbf{k}'} e^{i\theta^{(n)}_{\mathbf{k}'}} |1_{\mathbf{k}'}\rangle \tag{3}$$

where $\theta^{(n)}_{\mathbf{k}'}$ is a random phase chosen from a uniform distribution. It can be shown (see Supporting Information) that for a large N, the sum converges to the first-order correlation function.

$$G^{(1)}_{i,j}\left(\mathbf{r}_T, \mathbf{r}'_T\right) = \lim_{n\to\infty} \frac{1}{N} \sum_{n=1}^{N} \left\langle 0|\phi^{\dagger}_i(\mathbf{r}_T)|\mathbf{k}^{(n)}_{\text{rand}}\right\rangle \left\langle \mathbf{k}^{(n)}_{\text{rand}}|\phi_j\left(\mathbf{r}'_T\right)|0\right\rangle \tag{4}$$

While the value of this is initially zero, the SU(1,1) dynamics[43] of the operators mixes between the creation and annihilation operators (becoming superpositions of them), thus giving rise to nonzero values. Other expectation values that are quadratic in the field operators can be calculated in this manner, and in particular, the calculation of the second-order correlation function will be derived later, in Section 3. We conclude that in order to calculate the correlation function, we can sum over a large number N of photon wavefunctions[44] (c-number fields) $\langle \mathbf{k}^{(n)}_{\text{rand}}|\phi_j(\mathbf{r}'_T)|0\rangle$. We define the two terms in Equation (4) as

$$\begin{aligned} A^{\text{vac};(n)}_j(\mathbf{r}_T) &\equiv \left\langle 0|\phi_j(\mathbf{r}_T)|\mathbf{k}^{(n)}_{\text{rand}}\right\rangle \\ A^{\text{out};(n)}_j(\mathbf{r}_T) &\equiv \left\langle \mathbf{k}^{(n)}_{\text{rand}}|\phi_j(\mathbf{r}_T)|0\right\rangle \end{aligned} \tag{5}$$

Both these fields can be simulated as complex matrices, and can be understood as the vacuum fluctuations $(A^{\text{vac};(n)}_j(\mathbf{r}_T))$ and the generated signal\idler $(A^{\text{out};(n)}_j(\mathbf{r}_T))$ at a certain frequency. For measuring the correlation between two photons in different transverse modes $\mathbf{k}_T; \mathbf{k}'_T$ rather than two transverse positions $\mathbf{r}_T$ and $\mathbf{r}'_T$ (recall that we are calculating correlations at equal planes $z = z'$), these should be projected on an orthonormal basis, for instance, plane wave decomposition given by the Fourier transform $A^{\text{out\vac};(n)}_i(\mathbf{k}_T) = \text{FT}[A^{\text{out\vac};(n)}_j(\mathbf{r}_T)]$. Consequently, we can approximate[45] the first-order correlation in the wavevector representation as

$$G^{(1)}_{ij}\left(\mathbf{k}_T; \mathbf{k}'_T\right) \simeq \frac{1}{N} \sum_{n=1}^{N} \left[A^{\text{out};(n)}_i\left(\mathbf{k}_T\right)\right]^* \otimes A^{\text{out};(n)}_j\left(\mathbf{k}'_T\right) \tag{6}$$

where $\otimes$ is the outer (Kronecker) product $(A \otimes \text{B})_{i,j,k,l} = A_{i,j} \cdot B_{k,l}$. Note that the projection can be generalized to other orthonormal spatial bases (via modal decomposition), such as Hermite–Gauss or Laguerre–Gauss modes.

In order to derive equations for the evolution of the fields from Equation (5) along the nonlinear crystal, one needs first to solve the Heisenberg equations of motion for the SPDC Hamiltonian (see Supporting Information for more details), and then calculate the matrix element between the vacuum $|0\rangle$ and the random noise distribution $|\mathbf{k}_{\text{rand}}^{(n)}\rangle$. We consider SPDC, where a pump wave, with frequency ω_p and complex field amplitude A_p, spontaneously converts into two photons—signal and idler, with frequencies ω_s and ω_i, satisfying energy conservation via $\omega_p = \omega_s + \omega_i$. The pump is assumed to be strong relative to the generated fields, and thus is treated as a classical, undepleted coherent state. We obtain two pairs of coupled equations

$$
\begin{aligned}
i\frac{\partial A_i^{\text{out}}}{\partial z} &= -\frac{\nabla_\perp^2}{2k_i}A_i^{\text{out}} + \kappa_i e^{-i\Delta kz}\left(A_s^{\text{vac}}\right)^* \\
i\frac{\partial A_i^{\text{vac}}}{\partial z} &= -\frac{\nabla_\perp^2}{2k_i}A_i^{\text{vac}} + \kappa_i e^{-i\Delta kz}\left(A_s^{\text{out}}\right)^* \\
i\frac{\partial A_s^{\text{out}}}{\partial z} &= -\frac{\nabla_\perp^2}{2k_s}A_s^{\text{out}} + \kappa_s e^{-i\Delta kz}\left(A_i^{\text{vac}}\right)^* \\
i\frac{\partial A_s^{\text{vac}}}{\partial z} &= -\frac{\nabla_\perp^2}{2k_s}A_s^{\text{vac}} + \kappa_s e^{-i\Delta kz}\left(A_i^{\text{out}}\right)^*
\end{aligned}
\tag{7}
$$

where $\nabla_\perp^2$ is the transverse Laplacian; k_s, k_i are the wave vectors of the signal and idler, respectively; z is the propagation coordinate; $\kappa_{j=i,s}(\mathbf{r}) = \frac{\omega_j^2}{c^2 k_j}\chi^{(2)}(\mathbf{r})A_p$ is the coupling strength for the signal and the idler fields, where $\chi^{(2)}(\mathbf{r})$ is the (spatially varying) second-order susceptibility, c is the speed of light, and $\Delta k = k_p - k_s - k_i$ is the phase mismatch. These equations can be numerically solved similarly to the classical coupled wave equations, by using the split-step Fourier method.[46] The initial values of the fields given in Equation (5) are set to zero matrices ($A_j^{\text{out};(n)}$) and a white noise distribution with random phases ($A_j^{\text{vac};(n)}$). Physically, the quasi-probability distribution of the vacuum field is the Wigner function[47] with $n = 0$ photons, which reduces to a Gaussian function in phase-space.[48] Gaussian noise (white noise), has zero mean, suiting the physical description, nut vacuum also has nonzero variance $\langle \Delta E_{\text{vac}}^2 \rangle = \frac{\hbar\omega_j}{2\epsilon_0 n_j n_{gj} V}$, V denoting the quantization volume and $n_j, n_{g,j}$ are the refractive and group indices, respectively, for ω_j. Intuitively, this is equivalent to setting the power $P_j = 2n_j\epsilon_0 c\frac{V}{L}\langle \Delta E_{\text{vac}}^2 \rangle$ for the field A_j^{vac} (where L is the crystal length) to be consistent with the zero point quantum noise at $z = 0$:

$$
P = \frac{c}{n_{gj}L}\hbar\omega_j \tag{8}
$$

The advantage of the approach we present is that it enables, starting with a numerical realization of the vacuum noise, to calculate the statistical properties of the signal and idler output fields. This efficient calculation, using split-step Fourier, incorporates simultaneously the effects of diffraction and nonlinear coupling. Convergence of the first-order correlation is fast and requires only several iterations, which are independent of each other, so can be easily made parallel. Moreover, as will be shown in Section 3, the output fields and vacuum fields also enable to calculate the second order correlation function.

2.1. SPDC in a 2D Rectangular Nonlinear Photonic Crystal

2D periodically poled crystals[49,50] have been realized experimentally before in SPDC, based on either a rectangular lattice[11,12] or on a hexagonal lattice.[10,13] These crystals are attractive sources for the generation of beam-like path entangled photons. For the rectangular lattice, the entangled photons appear when the incident pump beam propagates in parallel to the photonic lattice axis, as can be readily calculated through wave-vector analysis of the reciprocal lattice (see **Figure 1**(b1)).

In order to demonstrate how this simulation method can be used to predict the output for crystals with spatially varying nonlinearity, we simulated SPDC in a 2D rectangular nonlinear photonic crystal. Changing the incidence angle will change the spatial output of the emitted light. In order to compare the simulated output with a spatially varying nonlinearity, we show new experimental results in Figure 1c of the spatial distribution of the emitted photon pairs in the Fourier plane for different incident angles. The experimental setup is identical to that reported in ref. [11] but with the crystal set at different angles with respect to the pump beam. The rectangular lattice was realized in a Mg-doped stoichiometric $LiTaO_3$ crystal,[51] with poling periods of 13.46 and 6.4 μm in the transverse and propagation directions, respectively. The nonlinear modulation was based on a circular motif having a radius of 2.7 μm in each lattice point. The pump used was a narrow linewidth diode laser with 35 mW at a wavelength of 404 nm. The signal and idler have the same wavelength of 808 nm, and were measured in the far field using a cooled sensitive camera, placed after a 3 nm bandpass filter centered at 808 nm.

In order to theoretically compute the SPDC far-field pattern, we used the derived expression of the first-order correlation function, Equation (6), for the degenerate case of $i = j, \mathbf{k}_T = \mathbf{k}'_T$, which is the autocorrelation of the (say signal) output field at frequency ω_s and specific wave vector k_s. Since the Kronecker product in Equation (6) squares the amount of memory needed (the computation for two $M \times M$ matrices yields a $M \times M \times M \times M$ matrix), for computing only the far-field pattern, we can directly compute the diagonal elements to reduce the memory necessary from $O(M^4)$ to $O(M^2)$. The far-field image converges quickly and is clearly evident after very few iterations. This configuration is very complex, and required high pixel resolution, as well as a long crystal ($M = 500$ and 5000 longitudinal steps), so each split-step Fourier iteration lasted ≈13 min on a standard PC (12 GB RAM). Figure 1d shows the simulated spatial distributions for the different incidence angles, for eight noise realizations. Clearly, excellent agreement can be found between the simulation and experiments, as presented in Figure 1c,d. Although the general trend of the emission pattern can be predicted geometrically using wave-vector considerations, our method provides much more information, as it reproduces the relative intensities and higher-order effects (detailed in the next sections), all in a single calculation. For more complex structures, such as aperiodic nonlinear photonic crystals,[5] these advantages become crucial for the correct calculation of the SPDC emission pattern.

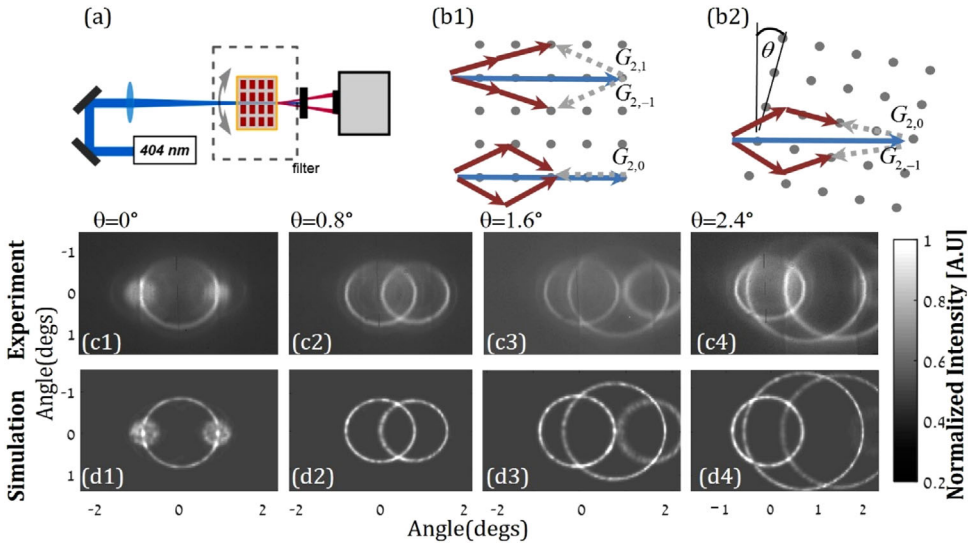

Figure 1. Simulation and experimental results for SPDC in a 2D rectangular nonlinear photonic crystal. a) Experimental setup. The crystal was rotated by an angle θ and the emission was measured at the Fourier plane. b) Reciprocal lattice representation of the crystal.[11] The Lattice constants are $a_1 = 6.4$ μm and $a_2 = 13.6$ μm. b1) For $\theta = 0°$, the top shows the $G_{2,1}$ and $G_{2,-1}$ process creating the beam entangled photons, and the bottom shows the parasitic $G_{2,0}$ process creating the outer ring. b2) Same for $\theta \neq 0°$. c) Experimental results and d) simulation results for varying values of θ.

3. Coincidences of SPDC Light: Second-Order Correlations

The second-order correlation function $G^{(2)}_{ijji}(\mathbf{k}_T, \mathbf{k}'_T; \mathbf{k}'_T, \mathbf{k}_T) = \langle \boldsymbol{a}^\dagger_i(\mathbf{k}_T)\boldsymbol{a}^\dagger_j(\mathbf{k}'_T)\boldsymbol{a}_j(\mathbf{k}'_T)\boldsymbol{a}_i(\mathbf{k}_T)\rangle$, denotes the probability of finding one i photon in mode $\mathbf{k}_T$ and another j photon in mode $\mathbf{k}'_T$. Experimentally, this quantity corresponds to the coincidence rate between these two photons. Since the Hamiltonian of SPDC is quadratic, and since vacuum is a Gaussian state, the resulting output state is also Gaussian, and in the general case corresponds to the multi-mode squeezed vacuum.[52] Conveniently, all higher moments of its Wigner function can be computed from the lowest order moments, namely the quadratic expectation values of the fields.[53] Specifically, we have that[54]

$$\begin{aligned}&\left\langle \boldsymbol{a}^\dagger_i\left(\mathbf{k}_T\right)\boldsymbol{a}^\dagger_j\left(\mathbf{k}'_T\right)\boldsymbol{a}_j\left(\mathbf{k}'_T\right)\boldsymbol{a}_i\left(\mathbf{k}_T\right)\right\rangle \\ &= \left\langle \boldsymbol{a}^\dagger_i\left(\mathbf{k}_T\right)\boldsymbol{a}_i\left(\mathbf{k}_T\right)\right\rangle\left\langle \boldsymbol{a}^\dagger_j\left(\mathbf{k}'_T\right)\boldsymbol{a}_j\left(\mathbf{k}'_T\right)\right\rangle \\ &\quad + \left|\left\langle \boldsymbol{a}^\dagger_i\left(\mathbf{k}_T\right)\boldsymbol{a}_j\left(\mathbf{k}'_T\right)\right\rangle\right|^2 + \left|\left\langle \boldsymbol{a}_i\left(\mathbf{k}_T\right)\boldsymbol{a}_j\left(\mathbf{k}'_T\right)\right\rangle\right|^2 \end{aligned} \tag{9}$$

So, after applying this rule:

$$\begin{aligned}G^{(2)}_{ijji}\left(\mathbf{k}_T, \mathbf{k}'_T; \mathbf{k}'_T, \mathbf{k}_T\right) &= G^{(1)}_{ii}\left(\mathbf{k}_T; \mathbf{k}_T\right) G^{(1)}_{jj}\left(\mathbf{k}'_T; \mathbf{k}'_T\right) + \left|G^{(1)}_{ij}\left(\mathbf{k}_T; \mathbf{k}'_T\right)\right|^2 \\ &\quad + \left|Q_{ij}\left(\mathbf{k}_T; \mathbf{k}'_T\right)\right|^2 \end{aligned} \tag{10}$$

where the first two terms on the right-hand side depend on the first-order correlation function and

$$Q_{ij}\left(\mathbf{k}_T; \mathbf{k}'_T\right) = \frac{1}{N}\sum_{n=1}^{N} A^{\text{vac}}_i\left(\mathbf{k}_T\right) \otimes A^{\text{out}}_j\left(\mathbf{k}'_T\right) \tag{11}$$

encompass the enhancement of the vacuum in the processes.

This calculation yields matrices the size of $M^2 \times M^2$ (or $M \times M \times M \times M$) due to the outer product, as should be expected for $G^{(2)}$. In most cases, some of the dimensions can be traced over to receive a 2D image which encompasses the main correlations, as will be outlined below in specific examples.

The algorithm of the simulation is now as follows: 1) Initialize the (structured) pump and (structured) crystal. 2) Initialize four $M \times M$ matrices: two zero matrices and two white noise distributions with variance according to Equation (8). 3) Solve Equation (7) using split-step Fourier. 4 Project the output fields on a desired orthonormal basis. 5) Calculate $Q^{(n)}_{ij}$ from Equation (11) and $G^{(1;n)}_{ij}$ from Equation (6), and add them to the accumulated value of each. Iterate over steps (2) to (5) for a large N number of times, each time setting a different random distribution for A^{vac}_j. 6) When finished iterating, reduce the matrix sizes by tracing over two dimensions of choice, and calculate $G^{(2)}_{ijji}$ according to Equation (10). A flow chart of the algorithm can be found in **Figure 2**. Each iteration (n) is independent of all other iterations; therefore, all N iterations can be run in parallel given a sufficient number of cores in order to speed up the simulation.

3.1. Correlations in a Degenerate SPDC Process in a 1D Periodically Poled Crystal

An instructive example of the method and its advantages with structured light would be to consider a type-0, frequency degenerate SPDC process in a periodically poled crystal with period Λ. In this process, momentum conservation dictates that the spontaneously generated photon pairs from a pump beam parallel to the optical axis, are emitted into a cone, concentric with the optical axis, wherein the far-field pattern corresponds to a circle (**Figure 3**a). The theoretical opening angle θ of the cone is

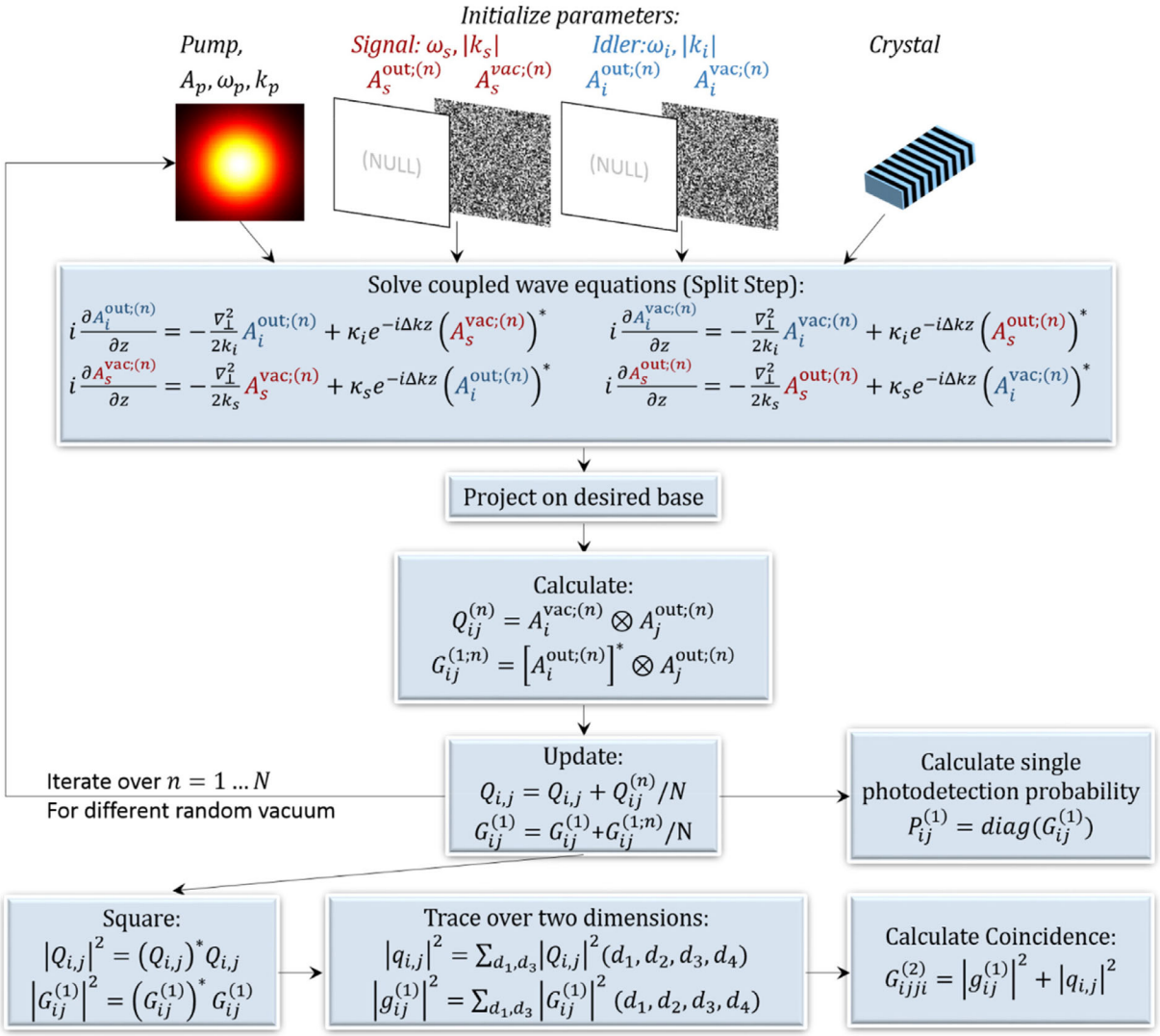

Figure 2. Schematic flow chart of the simulation procedure. The pump and crystal are determined initially and remain the same for all iterations. In each iteration, the initial signal (red) and idler (blue) output wavefunctions A^{out} are set to a zero $M \times M$ matrix, and the signal and idler vacuum wavefunctions A^{vac} are initialized as a (different) random white noise $M \times M$ matrix. The coupled wave equations are then solved using the Split Step Fourier method. The output solution is then projected on the desired base (Fourier transform, Hermite–Gauss, etc.). These are then used to calculate $Q_{i,j}$ and $G_{i,j}^{(1)}$, which are $M \times M \times M \times M$ large matrices. In each iteration, these two matrices are updated. After iterating N times, one can calculate the single photodetection probability, $P(k) = G_{i,j}^{(1)}(k, k)$, by taking the diagonal elements of $G_{i,j}^{(1)}$. For calculating the second order correlation, $G_{ijji}^{(2)}$, $Q_{i,j}$ and $G_{i,j}^{(1)}$ are first squared. After, $q_{i,j}$ and $g_{i,j}^{(1)}$, the reduced matrixes with dimensions $M \times M$, are calculated by tracing over two of their four dimensions d_1, d_3. Finally, they are summed to calculate the second-order correlation matrix.

determined by the phase-matching condition

$$\theta = \cos^{-1}\left(\frac{k_p - \frac{2\pi}{\Lambda}}{2k_s}\right) \tag{12}$$

For small pump powers, one may use first-order perturbation theory to obtain analytically the generated two-photon state, from which both the intensity pattern, $G^{(1)}$ (since $i = j$, we omit the indices), and the coincidence rate, $G^{(2)}$, could be derived.[42,55] A characteristic feature of these photons is their demonstration of anti-correlation: they are always emitted into opposite directions on the cone (see Figure 3b). This means that if one photon is detected on a specific point on the circle, its partner will be detected on the opposite side, with a 180° difference between their azimuthal angles. To demonstrate these features, we simulated such an SPDC process in a 5 mm long periodically poled lithium niobite (PPLN) crystal, with a 532 nm CW pump beam with a power of 5 mW and 100 µm waist. The far-field screen was imaged $R = 10$ cm away from the crystal, and the generated field amplitudes at 1064 nm were calculated. Since this is a simple configuration, we used relatively low resolution (80 × 80 pixels for each matrix, 5000 longitudinal steps). Unlike the first-order correlation which converges quickly, the second-order

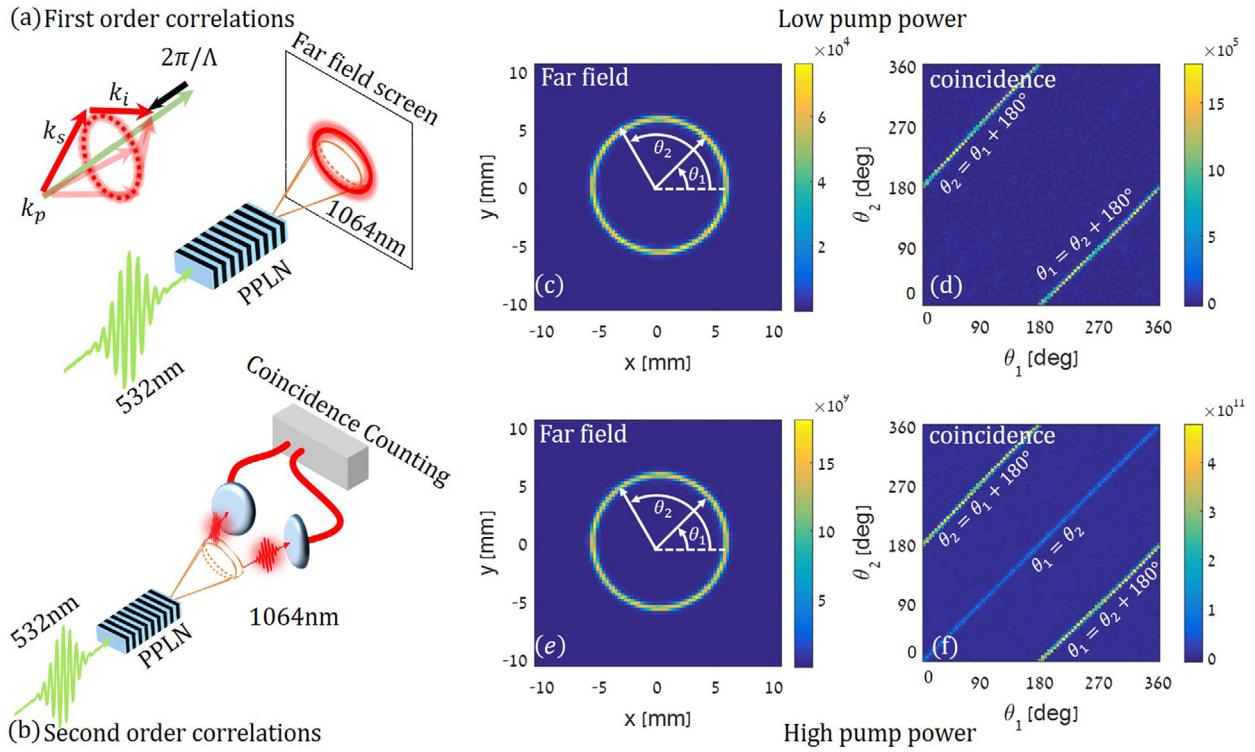

Figure 3. Simulation of degenerate SPDC in PPLN. a) The 532 nm input pump is converted to two 1064 nm signal and idler photons which form a ring in the far field due to momentum conservation, as depicted in the vector diagram. b) Second-order correlations are observed by coincidence counting of photons, collected at different azimuthal angles on the emission circle. c,d) The first order correlation $G^{(1)}(r_T, r_T)$ in the far field, simulated for c) a 5 mW pump power and d) a 1 kW pump peak power. The first-order correlation is normalized to yield the photodetection probability density per unit area, in units Hz mm^{-2}. Angles θ_1 and θ_2 are the azimuthal emission angles of signal and idler photons on the circle, with respect to the *x*-axis. e,f) The simulated second-order correlations, $G^{(2)}(\theta_1, \theta_2)$, for e) 5 mW pump power and f) 1 kW peak pump power. The second-order correlations are normalized to yield the coincidence rates per unit angle squared with respect to a coincidence window of $\tau = 1$ ns, in units of Hz rad^{-2}. Both (e) and (f) exhibit the expected coincidence peak along $|\theta_1 - \theta_2| = 180°$, whereas the strong pump (f) also demonstrates photon high order effects, as depicted by the $\theta_1 = \theta_2$ coincidence line.

correlation needs more iterations to converge, as it is directly dependent through $Q_{i,j}$ (Equation (11)) on the random fields. In order to compute it, we iterated over 300 random distributions, for a total of ≈42 min.

In Figure 3c, we plot $G^{(1)}(\mathbf{r}_T, \mathbf{r}_T)$ in far-field coordinates $\mathbf{r}_T = (R/k_0)\mathbf{k}_T$, with k_0 denoting the carrier wave number in free space, and $\mathbf{k}_T = (k_x, k_y)$ is the transverse Fourier frequency, where the emission circle can be clearly seen. In Figure 3c, $G^{(1)}(\mathbf{r}_T, \mathbf{r}_T)$ is normalized by the field amplitudes to yield the photodetection rate per unit area at the detection plane. Using Equation (10), we also plot $G^{(2)}(\theta_1, \theta_2; \theta_2, \theta_1)$ in Figure 3e, as a function of the two azimuthal emission angles on the circle, θ_1 and θ_2, defined in Figure 3c. We trace over the radial coordinates r and r' in order to reduce the matrix dimensions

$$G^{(2)}\left(\theta_1, \theta_2; \theta_2, \theta_1\right) = \sum_{r,r'} \left\{ G^{(1)}\left(r, \theta_1; r, \theta_1\right) G^{(1)}\left(r', \theta_2; r', \theta_2\right) + \left|G^{(1)}\left(r, \theta_1; r', \theta_2\right)\right|^2 + \left|Q\left(r, \theta_1; r', \theta_2\right)\right|^2 \right\} \tag{13}$$

The second-order correlation function is normalized to yield the coincidence rate with respect to a coincidence window of $\tau = 1$ ns. As expected, two distinct coincidence lines, corresponding to $|\theta_1 - \theta_2| = 180°$, can be observed. These lines demonstrate the photon spatial anti-correlation, as they can be detected at opposite azimuthal angles.

However, the first-order perturbation analysis fails[56,57] when strong pump peak powers are used, as higher-order effects become dominant. In this regime, the photons also demonstrate high order effects, that is, it is possible to detect two photons simultaneously at the same azimuthal angle. In that case, the approximations for $G^{(1)}$ and $G^{(2)}$ derived from the first-order generated state become inaccurate, and their approximate form to second-order in the perturbation cannot be derived analytically in a straightforward manner (actually, in this simple case, one can use instead the exact solution for the generated state, namely the multi-mode squeezed vacuum). In contrast, these correlations can be readily evaluated using our general, nonperturbative formalism. To demonstrate this, we repeated the same simulations but this time with a dramatically increased pump peak power of 1 kW. The emission pattern of $G^{(1)}$, depicted in Figure 3e, does not show any significant difference other than a higher brightness due to the higher conversion rate. However, for $G^{(2)}$, an additional coincidence line corresponding to $\theta_1 = \theta_2$ can be clearly seen in Figure 3f. This new feature indeed demonstrates the anticipated high order effect at higher

pump powers. Although the above analysis is intuitive for this simple example, once non-trivial structures are considered, it is clear why our formalism can be highly beneficial for the accurate calculation of SPDC correlations in any pumping regime. A Python code showing this example is available in Supporting Information.

4. SPDC with Structured Beams

4.1. SPDC with Hermite–Gauss Pump Beams

An important family of structured beams are the Hermite Gaussian (HG) modes. These modes are solutions to the paraxial Helmholtz equation in Cartesian coordinates, and are eigenstates of the free space propagator. Thus, they maintain their shape when propagating (up to a magnification factor owing to diffraction), and form a complete discrete basis. An interesting result concerning these modes[22,58,59] shows that the modal number obeys conservation laws, leading to high orders of entanglement. Following previous works,[22,58,59] we consider a nonlinear crystal pumped with the following HG beam profile:

$$E_p^{n,m}\left(\mathbf{r}_T, w_p\right) = \mathrm{HG}_n\left(x, w_p\right)\mathrm{HG}_m\left(y, w_p\right) \tag{14}$$

where x, y are the transverse coordinates, w_p is the pump waist, and HG_i are the HG modes of order i.[60] Being a complete basis, the generated bi-photon state can be decomposed into discrete HG signal and idler modes.

$$|\psi^{n,m}\rangle = \sum_{j,l,u,t=0}^{\infty} C_{j,l,u,t}^{(n,m)} |\mathrm{HG}_{j,l}, \sigma_s\rangle_s |\mathrm{HG}_{u,t}, \sigma_i\rangle_i \tag{15}$$

with $\sigma_{i,s}$ denoting the waists of the down converted HG idler and signal, and for abbreviation, we use HG_{jl} to denote an HG mode of order j in the x axis and of order l in the y axis. Under the paraxial approximation, and if one models the bi-photon amplitude using a separable function such as a Gaussian (see refs. [22,58,59,61] for more details), then the coefficients $C_{j,l,u,t}^{(n,m)}$ are also separable (with respect to the two axes) $C_{j,l,u,t}^{(n,m)} = c_{j,u}^{(n)} c_{l,t}^{(m)}$. Furthermore, interesting states (such as Bell states) can be obtained for a certain choice of the beam waist σ. This result has been experimentally confirmed by Kovlakov et al.,[22] who used a periodically poled crystal pumped with an HG-shaped pump beam, and measured the output state projected on the HG basis. The down-converted photon modes were determined using diffraction from an SLM. This method enables the generation of Bell states without need for post-selection.

We performed a simulation following this experiment. Here, a 25 mm PPKTP crystal is pumped with a 407 nm laser having a waist of ≈30 μm, shaped into $\mathrm{HG}_{0,n}$ modes, with $n = 0, 1, 2$. The process considered was a type II frequency degenerate (i.e., signal and idler have the same 814 nm wavelength) SPDC which enables a simple separation of the signal and idler via their polarization. Each output field was decomposed into the HG basis by projecting the field on HG modes, up to $n, m = 50$, via (here, HG modes are normalized to unity)

$$c_{i,j}^{(n)} = \frac{1}{\iint \left|A^{\mathrm{out}}(\mathbf{r}_T)\right|^2 d^2\mathbf{r}_T} \iint \mathrm{HG}_{\mathrm{i,j}}^{*}(\mathbf{r}_T) A^{\mathrm{out}}(\mathbf{r}_T) d^2\mathbf{r}_T, \tag{16}$$

where $c_{i,j}^{(n)}$ gives the normalized mode weights and satisfies the normalization condition: $\sum_{i,j} |c_{i,j}^{(n)}|^2 = 1$. Finally, for second-order correlations in the Hermite Gauss basis $G^{(2)}(\mathrm{HG}_j, \mathrm{HG}_u; \mathrm{HG}_u, \mathrm{HG}_j)$, we traced over the vertical axis in a similar manner to Equation (13) (with r, r', replaced by $\mathrm{HG}_l(y), \mathrm{HG}_t(y')$ and θ_1, θ_2 replaced by $\mathrm{HG}_j(x), \mathrm{HG}_u(x')$) to receive $G^{(2)} = \sum_{l,t} |C_{j,l,u,t}^{(n,0)}|^2 = \sum_{l,t} |c_{j,u}^{(n)}|^2 |c_{l,t}^{(0)}|^2 = |c_{j,u}^{(n)}|^2$, corresponding to the horizontal modes relative coincidence rates.

We successfully recover the experimental results of ref. [22], which can be seen, for example, by comparing **Figure 4**b with Figure 2 in ref. [22] where the expected off-diagonal second-order correlations of the Bell state are clearly evident.

4.2. SPDC with Laguerre–Gauss Beams

Another interesting basis to follow is that of the Laguerre–Gauss (LG_{pl}) modes, which are solutions of the paraxial Helmholtz equation, but this time in cylindrical coordinates, with radial and azimuthal indices p and l, respectively. For every nonzero l, the beams are vortices carrying $\hbar l$ orbital angular momentum (OAM). These modes are particularly interesting due to their high capacity for quantum information, as well as their potential use for generating high-dimensional entanglement.[27,62–64] The SPDC process in transversely uniform nonlinear crystals has been shown[24] to conserve OAM between the interacting fields, such that $l_{\mathrm{signal}} + l_{\mathrm{idler}} = l_{\mathrm{pump}}$.

The simulation we present in **Figure 5** follows the seminal experiment by Mair et al.,[24] the first to demonstrate entanglement through OAM conservation. The experiment was done using a type-I degenerate SPDC with a 351 nm pump beam (signal and idler at 702 nm), in a 1.5 mm thick BBO crystal. For the simulation, we initialized the pump beam in LG modes with OAM of $l_{\mathrm{pump}} = 1, 3, -4, 10$, in order to show the versatility of the conservation law. The output field again was projected onto the LG basis using Equation (16) (and exchanging HG by LG). We traced over the radial index of the LG modes using Equation (13) (replacing r, r' by $\mathrm{LG}_p, \mathrm{LG}_{p'}$ and θ_1, θ_2 by $\mathrm{LG}_{l_{\mathrm{signal}}}, \mathrm{LG}_{l_{\mathrm{idler}}}$) in order to extract the second-order correlation function, $G^{(2)}(l_{\mathrm{signal}}, l_{\mathrm{idler}})$, which is dependent on the OAM topological charges of the signal and idler, l_{signal} and l_{idler}, respectively. OAM conservation is evident from the results in Figure 5c, as a clear coincidence line, each time shifted by exactly the pump's topological charge.

Generation of OAM carrying SPDC photons can be extended to structured crystals having an edge dislocation, which were shown to carry quasi OAM.[65–67] Such a dislocation results in a fork shaped pattern, where the upper half of the crystal has l_c extra transverse periods with respect to the lower part, thereby creating a fork shape around the center singularity point. These

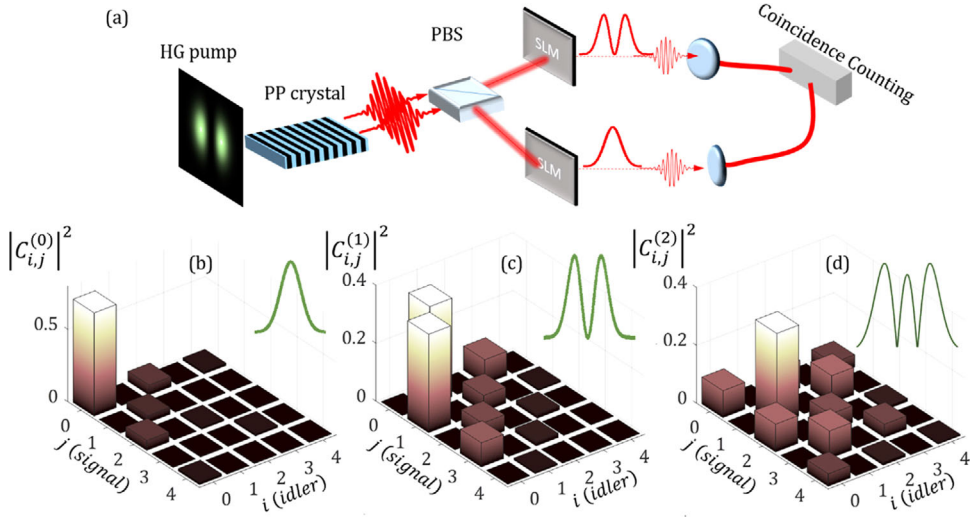

Figure 4. Simulations of second-order correlations for SPDC with a Hermite–Gauss pump beam. a) Schematic representation of the experiment: the pump beam is shaped as an HG mode and illuminates a periodically poled (PP) KTP crystal, phase matched for a type II process. The output photons are separated by a polarizing beam splitter (PBS), each then projected on an SLM for mode sorting. The output modes (HG modes) are coupled to detectors for coincidence counting. The pump is shaped as HG 00 (b), 01 (c), and 02 (d), as a function of the horizontal modal number of the signal and idler. The simulations recover the experimental results reported in ref. [22].

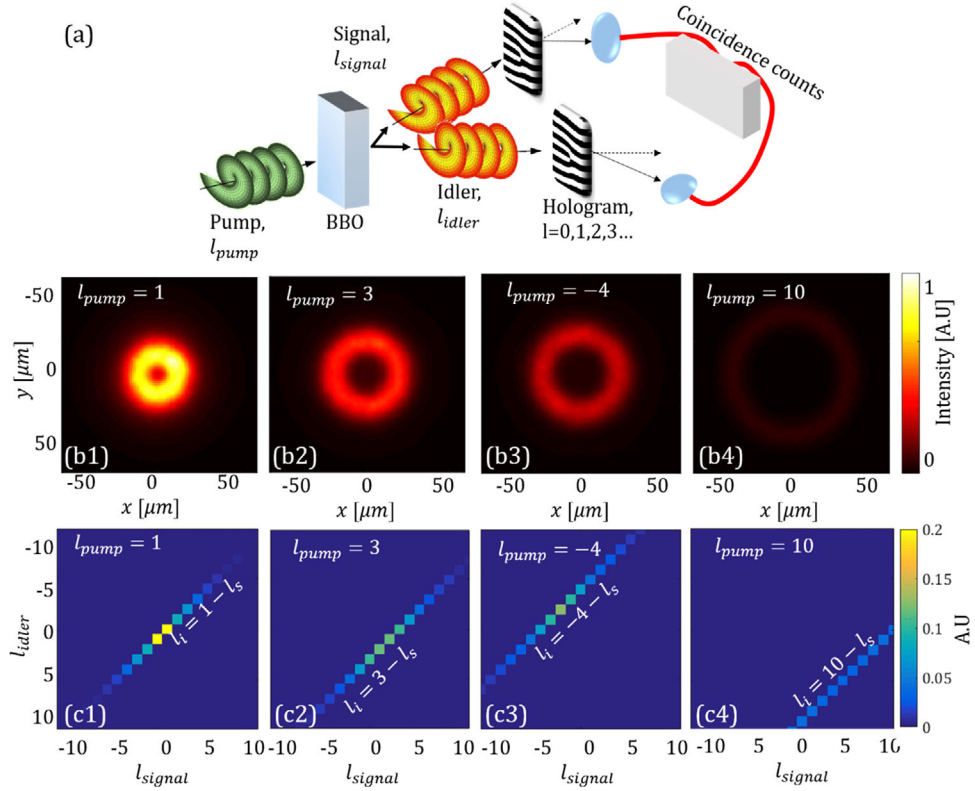

Figure 5. Simulations of first- and second-order correlations for SPDC with a Laguerre–Gauss shaped pump beam in a transversely uniform nonlinear crystal (BBO). a) Experimental setup: a 351 nm pump beam with OAM of $\hbar l_{pump}$ is injected into a BBO crystal. Signal and idler photons at 702 nm with OAM of $\hbar l_{signal}$ and $\hbar l_{idler}$ emerge. Coincidences are observed by projecting onto different LG modes using holograms. b1–b4) Simulated near-field first-order correlation $G^{(1)}(r, r')$ for an input pump $l_{pump} = 1, 3, -4, 10$, respectively. c1–c4) Second-order correlation $G^{(2)}(l_{signal}, l_{idler})$ for $l_{pump} = 1, 3, -4, 10$. OAM is conserved in the process, that is, $l_{signal} + l_{idler} = l_{pump}$, so the coincidence takes the form of straight, parallel, lines, shifted by l_{pump}.

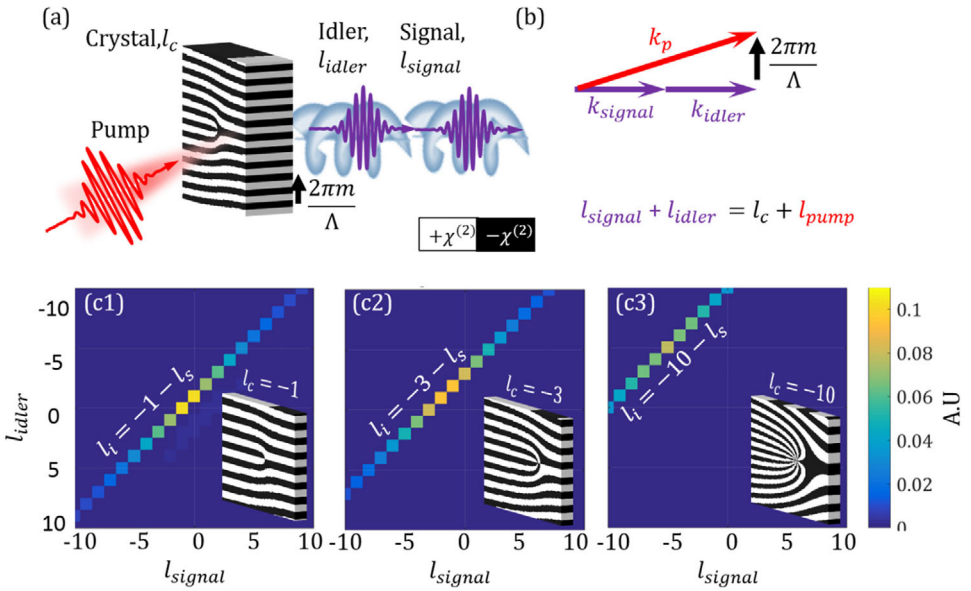

Figure 6. Simulations of second-order correlations for type 0 SPDC with a fork-shaped crystal. a) Experimental setup: 780 nm Gaussian pump beam is injected into a $LiNbO_3$ crystal with a fork-shaped transverse poling pattern of different topological charges, with a transverse period of $\Lambda = 1.98$ μm. The beam is inserted at an angle which corresponds to the first diffraction order $m = 1$. Signal and idler beams at 1560 nm, emerge co-linearly from the crystal with OAM of $\hbar l_{signal}$ and $\hbar l_{idler}$. b) Vector diagram of the process, $\boldsymbol{k}_p$, $\boldsymbol{k}_s$, $\boldsymbol{k}_i$ are the wave vectors of the pump, signal, and idler, respectively. c1–c3) Simulated second-order correlation $G^{(2)}(l, l')$ for $l_c = -1, -3, -10$. Quasi-OAM is conserved in the process, $l_{signal} + l_{idler} = l_{pump} + l_c$, so the coincidence matrix takes the form of straight, parallel, lines, shifted by l_c ($l_{pump} = 0$).

fork-shaped crystals add their quasi-OAM, thereby providing a modified OAM conservation rule:

$$l_{signal} + l_{idler} = l_{pump} + ml_c \tag{17}$$

where $\hbar l_c$ is the quasi-OAM of the crystal, and m is the diffraction order. This type of configuration was suggested to create a two-photon N00N states using single photons carrying OAM[33] in the $m = 1$ and $m = -1$ diffraction orders. We follow theoretical work[34] on fork-shaped crystals to show that Equation (17) is evident from the second-order correlations simulated by our program. A 780 nm Gaussian pump beam is inserted at an angle θ into a 0.5 mm thick $LiNbO_3$ crystal with a forked shape transverse poling pattern of differing topological charge, $\chi^{(2)}(x, y) = \text{sign}[\cos(\frac{2\pi}{\Lambda}x + l_c\varphi(x, y))]$, where x, y are the transverse coordinates, $\varphi(x, y) = \tan^{-1}(y/x)$ is the polar coordiant, and Λ is the transverse period. The period Λ and the angle of the input pump were determined by solving the wave vector diagram, as depicted in **Figure 6b**.

$$\begin{aligned} k_p \sin(\theta) &= \frac{2\pi}{\Lambda} \\ k_p \cos(\theta) - k_s - k_i &= 0 \end{aligned} \tag{18}$$

which results in a period of $\Lambda = 1.98$ μm, at an angle θ =10.6°. The pump waist was chosen for optimal coupling, that is, $w_p = \sqrt{L/k_p} = 5.4$ μm. Decomposition of the output was preformed for $-20 \le l \le 20$ and $0 < p \le 20$ modes, with p denoting the radial mode number, and iterated over 300 different input noise realizations. The results in Figure 6c–e show a clear straight line as a function of the signal and idler azimuthal indices, which corresponds to the conservation law, Equation (17), with $l_{pump} = 0$ and for different quasi OAM.

5. Conclusion

In summary, we have demonstrated a simulation tool for the calculation of SPDC first- and second-order correlations, in the presence of sophisticated structures of the pump beam and/or nonlinear photonic crystal. Being nonperturbative, our method is valid for all pumping regimes, as opposed to the commonly employed first-order perturbation analysis which fails, for example, when high peak-power pulsed lasers are used. While our computation included only second-order coupling, one can extend this work to other high order effects such as cross phase modulation,[68] as long as the Hamiltonian stays quadratic. As a proof of concept, we examined a wide range of structured light beams and structured crystals for which our simulation correctly reproduces the experimentally measured SPDC correlations or the theoretically calculated ones. For 2D nonlinear photonic crystals at different angles with respect to the optical axis, we recover new unpublished experimental results for the emission pattern, surpassing the simple wave-vector considerations commonly used for evaluating the output state. In addition, we recover the expected conservation laws for the optical modes in both the Hermite–Gauss basis (where we reproduce the experimental results of ref. [22]), as well as in the Laguerre–Gauss basis (where we recover the experiment in ref. [24] and the theoretical predictions in ref. [34]). Whereas here we considered spatial correlations of single frequency beams, our method can be

easily extended to handle broad frequency sources and nonlinear crystals for spectral shaping,[69–73] thereby enabling to design and analyze spectral correlations, for example, the joint spectral amplitude in SPDC process, as well as prospects for frequency and spatial correlations.[74–77] This formalism can be generalized for other Gaussian states, such as thermal light and squeezed coherent states.[78] All our analysis is based on the paraxial formalism of quantum optics[42] (see Supporting Information), which is suitable for almost all experimental implementations in bulk crystals. Extending this formalism outside the paraxial approximation will require much greater computational complexity (in time and memory), for example in waveguides and resonators.

Our method can facilitate the design of complex crystal structures and spatially varying input pump beams in order to arbitrarily shape down-converted photons and control higher-order correlations. An example of Python code for this method can be found in Supporting Information. Please acknowledge this work if using the code for simulations.

Supporting Information

Supporting Information is available from the Wiley Online Library or from the author.

Acknowledgements

This study was supported by Israel Science Foundation, grant nos. 1415/17 and 2085/18. S.T.-M. was supported by the Ministry of Science women in science scholarship. A.K. was supported by the Adams fellowship of the Israel Academy in Science and Humanities. N.V.-B. is a Lady-Davis fellowship trust scholar. The authors thank Prof. Robert W. Boyd and Prof. Mark Shtaif for stimulating discussions.

Conflict of Interest

The authors declare no conflict of interest.

Keywords

nonlinear optics, quantum optics, spontaneous parametric down-conversion, structured light, vortex beams

Received: September 24, 2019
Revised: January 6, 2020
Published online: February 10, 2020

[1] T. Jennewein, C. Simon, G. Weihs, H. Weinfurter, A. Zeilinger, *Phys. Rev. Lett.* **2000**, *84*, 4729.
[2] I. Marcikic, H. de Riedmatten, W. Tittel, H. Zbinden, M. Legré, N. Gisin, *Phys. Rev. Lett.* **2004**, *93*, 180502.
[3] C.-Y. Lu, D. E. Browne, T. Yang, J.-W. Pan, *Phys. Rev. Lett.* **2007**, *99*, 250505.
[4] R. W. Boyd, *Nonlinear Optics*, Academic Press, San Diego, CA **2008**.
[5] A. Arie, N. Voloch, *Laser Photonics Rev.* **2010**, *4*, 355.
[6] S. Trajtenebrg-Mills, I. Juwiler, A. Arie, *Laser Photonics Rev.* **2015**, *9*, L40.
[7] S. Trajtenebrg-Mills, A. Arie, *Opt. Mater. Express* **2017**, *7*, 2928.
[8] J. P. Torres, A. Alexandrescu, S. Carrasco, L. Torner, *Opt. Lett.* **2004**, *29*, 376.
[9] H. Y. Leng, P. Xu, Z. D. Xie, H. Jin, C. Zhang, S. N. Zhu, *Nat. Commun.* **2011**, *2*, 429.
[10] H. Jin, P. Xu, X. W. Luo, H. Y. Leng, Y. X. Gong, W.J Yu, M. L. Zhong, G. Zhao, S. N. Zhu, *Phys. Rev. Lett.* **2013**, *111*, 023603.
[11] E. Megidish, A. Halevy, H. S. Eisenberg, A. Ganany-Padowicz, N. Habshoosh, A. Arie, *Opt. Express* **2013**, *21*, 6689.
[12] X. W. Luo, P. Xu, C. W. Sun, H. Jin, R. J. Hou, H. Y. Leng, S. N. Zhu, *J. Opt.* **2017**, *19*, 065201.
[13] L. Chen, P. Xu, Y. F. Bai, X. W. Luo, M. L. Zhong, M. Dai, M. H. Lu, S. N. Zhu, *Opt. Express* **2014**, *22*, 13164.
[14] S. P. Walborn, C. H. Monken, S. Pádua, P. H. Souto Ribeiro, *Phys. Rep.* **2010**, *495*, 87.
[15] C. H. Monken, P. H. S. Ribeiro, S. Pádua, *Phys. Rev. A* **1998**, *57*, 3123.
[16] G. Molina-Terriza, S. Minardi, Y. Deyanova, C. I. Osorio, M. Hendrych, J. P. Torres, *Phys. Rev. A* **2005**, *72*, 065802.
[17] J.-C. Lee, Y.-H. Kim, *Opt. Commun.* **2016**, *366*, 442.
[18] R. S. Bennink, *Phys. Rev. A* **2010**, *81*, 053805.
[19] A. Valencia, A. Ceré, X. Shi, G. Molina-Terriza, J. P. Torres, *Phys. Rev. Lett.* **2007**, *99*, 243601.
[20] S. P. Walborn, A. N. de Oliveira, R. S. Thebaldi, C. H. Monken, *Phys. Rev. A* **2004**, *69*, 023811.
[21] G. A. Barbosa, *Phys. Rev. A* **2007**, *76*, 033821.
[22] E. V. Kovlakov, I. B. Bobrov, S. S. Straupe, S. P. Kulik, *Phys. Rev. Lett.* **2017**, *118*, 030503.
[23] J. Romero, D. Giovannini, M. G. McLaren, E. J. Galvez, A. Forbes, M. J. Padgett, *J. Opt.* **2012**, *14*, 085401.
[24] A. Mair, A. Vaziri, G. Weihs, A. Zeilinger, *Nature* **2001**, *412*, 313.
[25] A. Vaziri, G. Weihs, A. Zeilinger, *Phys. Rev. Lett.* **2002**, *89*, 240401.
[26] M. Malik, M. Erhard, M. Huber, M. Krenn, R. Fickler, A. Zeilinger, *Nat. Photonics* **2016**, *10*, 248.
[27] G. Molina-Terriza, J. P. Torres, L. Torner, *Nat. Phys.* **2007**, *3*, 305.
[28] G. Molina-Terriza, J. P. Torres, L. Torner, *Phys. Rev. Lett.* **2002**, *88*, 013601.
[29] L. A. Lugiato, A. Gatti, E. Brambilla, *J. Opt. B: Quantum Semiclassical Opt.* **2002**, *4*, S176.
[30] D. Ljunggren, M. Tengner, *Phys. Rev. A* **2005**, *72*, 062301.
[31] W. P. Grice, R. S. Bennink, D. S. Goodman, A. T. Ryan, *Phys. Rev. A* **2011**, *83*, 023810.
[32] X. Chen, P. Karpinski, V. Shvedov, A. Boes, A. Mitchell, W. Krolikowski, Y. Sheng, *Opt. Lett.* **2016**, *41*, 2410.
[33] Y. Ming, J. Tang, Z. x. Chen, F. Xu, L. j. Zhang, Y. q. Lu, *IEEE J. Sel. Top. Quantum Electron.* **2015**, *21*, 3.
[34] L. L. Lu, P. Xu, M. L. Zhong, Y. F. Bai, S. N. Zhu, *Opt. Express* **2015**, *23*, 1203.
[35] S. P. Walborn, C. H. Monken, *Phys. Rev. A* **2007**, *76*, 062305.
[36] G. A. Barbosa, *Phys. Rev. A* **2009**, *80*, 063833.
[37] R. Saaltink, L. Giner, R. Boyd, E. Karimi, J. Lundeen, *Opt. Express* **2016**, *24*, 24495.
[38] H. Defienne, S. Gigan, *Phys. Rev. A* **2019**, *99*, 053831.
[39] E. Brambilla, A. Gatti, M. Bache, L. A. Lugiato, *Phys. Rev. A* **2004**, *69*, 023802.
[40] E. Lantz, N. Treps, C. Fabre, E. Brambilla, *Eur. Phys. J. D - At. Mol. Opt. Phys.* **2004**, *29*, 437.
[41] G. D. Jimenez, V. G. Garces, K. A. O'Donnell, *Phys. Rev. A* **2017**, *96*, 023828.
[42] J. Garrison, R. Chiao, *Quantum Optics*, Oxford University Press, Oxford **2008**.
[43] B. Yurke, S. L. McCall, J. R. Klauder, *Phys. Rev. A* **1986**, *33*, 4033.
[44] G. Grynberg, A. Aspect, C. Fabre, *Introduction to Quantum Optics: From the Semi-classical Approach to Quantized Light*, Cambridge University Press, Cambridge **2010**.

[45] In practice, photon count rates are never limited to a single frequency, and measurements are taken for some spectral width $\Delta\omega$. In order to compute the count rate, one must perform the simulation multiple times for different frequencies within the bandwidth $\Delta\omega$. Alternately, for an estimate of the rates, one can multiply by a unit less factor which embodies the time the photon spent inside the crystal (nL/c) and a first-order derivation of $\Delta k(\frac{1}{\sqrt{v_{GVD}\,L}})$ for type 0 and 1, $(\frac{nL}{c})/\sqrt{v_{GVm}L}$ for type 2; for more details, see ref. [50].
[46] G. Agrawal, *Nonlinear Fiber Optics*, 3rd ed., Academic Press, San Diego, CA **2001**.
[47] E. Wigner, *Phys. Rev.* **1932**, *40*, 749.
[48] W. Schleich, *Quantum Optics in Phase Space*, Wiley-VCH, Weinheim **2001**.
[49] A. Arie, N. Habshoosh, A. Bahabad, *Opt. Quantum Electron.* **2007**, *39*, 361.
[50] V. Berger, *Phys. Rev. Lett.* **1998**, *81*, 4136.
[51] I. Dolev, A. Ganany-Padowicz, O. Gayer, A. Arie, J. Mangin, G. Gadret, *Appl. Phys. B* **2009**, *96*, 423.
[52] A. Ferraro, S. Olivares, M. G. A. Paris, arXiv:0503237[quant-ph], **2005**.
[53] C. Gardiner, *Quantum Noise*, Springer, Berlin **1991**.
[54] C. W. Crispin, W. Gardiner, P. (Peter) Zoller, *Quantum Noise: A Handbook of Markovian and Non-Markovian Quantum Stochastic Methods with Applications to Quantum Optics*, Springer, Berlin **2004**.
[55] J. Schneeloch, S. H. Knarr, D. F. Bogorin, M. L. Levangie, C. Tison, R. Frank, G. Howland, M. Fanto, P. Alsing, *J. Opt.* **2019**, *21*, 043501.
[56] W. Mauerer, M. Avenhaus, W. Helwig, C. Silberhorn, *Phys. Rev. A* **2009**, *80*, 053815.
[57] W. Wasilewski, C. Radzewicz, R. Frankowski, K. Banaszek, *Phys. Rev. A* **2008**, *78*, 033831.
[58] S. P. Walborn, S. Pádua, C. H. Monken, *Phys. Rev. A* **2005**, *71*, 053812.
[59] S. P. Walborn, A. H. Pimentel, *J. Phys. B: At. Mol. Opt. Phys.* **2012**, *45*, 165502.
[60] B. E. A. Saleh, M. C. Teich, *Fundamentals of Photonics*, Wiley, New York **2013**.
[61] X. F. Ren, G. P. Guo, J. Li, G. C. Guo, *Phys. Lett. A: Gen. At. Solid State Phys.* **2005**, *341*, 81.
[62] M. Erhard, R. Fickler, M. Krenn, A. Zeilinger, *Light Sci. Appl.* **2018**, *7*, 17146.
[63] M. Krenn, M. Malik, M. Erhard, A. Zeilinger, *Philos. Trans. R. Soc. A: Math. Phys. Eng. Sci.* **2017**, *375*, 20150442.
[64] M. J. Padgett, *Opt. Express* **2017**, *25*, 11265.
[65] N. V. Bloch, K. Shemer, A. Shapira, R. Shiloh, I. Juwiler, A. Arie, *Phys. Rev. Lett.* **2012**, *108*, 233902.
[66] K. Shemer, N. Voloch-Bloch, A. Shapira, A. Libster, I. Juwiler, A. Arie, *Opt. Lett.* **2013**, *38*, 5470.
[67] S. Sharabi, N. Voloch-Bloch, I. Juwiler, A. Arie, *Phys. Rev. Lett.* **2014**, *112*, 053901.
[68] Z. Vernon, J. E. Sipe, *Phys. Rev. A* **2015**, *91*, 053802.
[69] A. M. Brańczyk, A. Fedrizzi, T. M. Stace, T. C. Ralph, A. G. White, *Opt. Express* **2011**, *19*, 55.
[70] A. Dosseva, Ł. Cincio, A. M. Brańczyk, *Phys. Rev. A* **2016**, *93*, 013801.
[71] P. Ben Dixon, J. H. Shapiro, F. N. C. Wong, *Opt. Express* **2013**, *21*, 5879.
[72] R. Shiloh, A. Arie, *Opt. Lett.* **2012**, *37*, 3591.
[73] A. Leshem, R. Shiloh, A. Arie, *Opt. Lett.* **2014**, *39*, 5370.
[74] A. Karnieli, S. Trajtenberg-Mills, G. Di Domenico, A. Arie, *Optica* **2019**, *6*, 1401.
[75] A. Karnieli, A. Arie, *Opt. Express* **2018**, *26*, 4920.
[76] A. Karnieli, A. Arie, *Phys. Rev. Lett.* **2018**, *120*, 053901.
[77] A. Karnieli, A. Arie, *Optica* **2018**, *5*, 1297.
[78] O. Scully, M. S. Zubairy, *Quantum Optics*, Cambridge University Press, Cambridge **1997**.
[79] C. K. Hong, L. Mandel, *Phys. Rev. A* **1985**, *31*, 2409.